13 Phase transitions and superconducting photon detectors

A. Gazizulina, X. Zhang, F. von Rohr, H. Grundmann, S. Siegrist, A. Engel and A. Schilling

in collaboration with: University of Bern (K. Krämer), Karlsruhe Institut für Technologie (K. Il'in), Deutsches Zentrum für Luft- und Raumfahrt (H.-W. Hübers, A. Semenov), University of Wellington (E. Anton, B. Ruck), Leiden University (J. Renema, M. van Exter, M. de Dood), University of Geneva (F. Bussieres, H. Zbinden), FIRST Lab ETH Zürich, PSI Villigen (M. Medarde, K. Conder), McMaster University (H. Dabkowska), IFW Dredsen (V. Kataev, A. Alfonsov), High Field Magnet Laboratory Nijmegen (L. Peters), Hochfeld-Magnetlabor Dresden-Rossendorf (T. Förster), University of S ao Paulo (A. Paduan-Filho), Institute of Nuclear Physics, Tashkent (A. Rakhimov), ETH Zürich (R. Nesper & J. Novotny), Princeton University (R. J. Cava)

(PTMA)

In the past few years, a growing number of superconducting materials have been suggested for use in Superconducting nanowire single-photon detectors (SNSPD), including amorphous materials, see for example [1]. Amorphous films are interesting because they are easier to fabricate on a larger variety of substrates, since no close matching between the two crystal structures is necessary. Amorphous films can also be more easily integrated into more complex micro- and nanostructures, such as optical cavities or multilayers, because they typically do not require elevated substrate temperatures during film deposition. Therefore they are more likely to be compatible with other materials and lithographic technologies. Last but not least, one can expect more homogeneous films and nanostructures on length scales from a few nanometers to micrometers because there are no grain boundaries, for example. W_xSi_{1-x} is particularly interesting as a material for X-SNSPD because of the good X-ray absorption properties of W which has motivated us to investigate W_xSi_{1-x} films of different composition and thickness.

The W_xSi_{1-x} films were prepared by co-sputtering of pure W and Si targets in an Ar atmosphere at room temperature. The deposition parameters have been optimized to obtain maximum T_c for thin (down to 5 nm) and thick films ($>$ 100 nm) and varying composition $0.15 \leq x \leq 0.3$. The resulting film thicknesses have been measured with a step-profiler and an AFM from which we calculated the deposition rates. The compositions of the films have been verified with EDX. We are now able to produce W_xSi_{1-x} films with the desired thickness and composition with high reproducibility. The measured T_c values of thick and thin films compare favorably with published data [2, 3]. A comprehensive set of normal-state and superconducting material parameters were determined from magneto-conductivity measurements as shown in Fig. 13.1, which are important for the design and the operation of SNSPD and X-SNSPD [4]. Typical values for the most important parameters are given in Table 13.1, together with values for NbN and TaN films.

The knowledge of the W_xSi_{1-x} material parameters allowed us to apply our recently developed detection model [5, 6]. We have found strong indications that in W_xSi_{1-x} a much lower energy (corresponding to mid-infrared photons) is necessary to completely suppress superconductivity in a significant part of the strip cross-section. The enhanced sensitivity to low-energy photons is a consequence of the reduced T_c and the lower density of states of W_xSi_{1-x} as compared to NbN and may explain some of the peculiar differences between W_xSi_{1-x} and nitride based SNSPD [6].

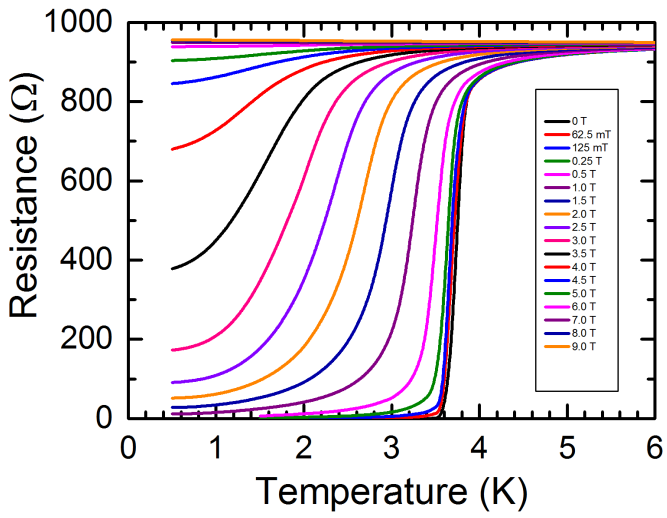

FIG. 13.1 – Resistance as a function of temperature and magnetic field for a typical $W_{0.8}Si_{0.2}$ film of 10 nm thickness.

TAB. 13.1 –
Summary of the most important material parameters of a typical thin $W_{0.8}Si_{0.2}$ film compared to the respective parameters of similarly thick NbN and TaN films.

Material	Energy gap (meV)	Coherence length (nm)	Penetration depth (nm)	Diffusion coefficient (nm^2/ps)
NbN	2.3	4.2	430	52
TaN	1.3	5.2	520	60
WSi	0.53	8.0	1400	75

[1] V. B. Verma *et al.*, Appl. Phys. Lett., **105**, (2014) 022602.

[2] S. Kondo, J. Mater. Res., **7**, (1992) 853.

[3] B. Baek *et al.*, Appl. Phys. Lett., **98**, (2011) 251105.

[4] J. Lonsky, Bachelor thesis, Universität Zürich (2014).

[5] A. Engel and A. Schilling, J. Appl. Phys., **114**, (2013) 214501.

[6] A. Engel, J. Lonsky, X. Zhang, and A. Schilling, IEEE Trans. Appl. Supercon. **25**, (2015) 2200407.

13.1 Influence of doping on the BEC-phase boundary in $Ba_{3-x}Sr_xCr_2O_8$

In the previous annual report, we described how chemical disorder influences the structure and magnetic interactions in the solid solution $Ba_{3-x}Sr_xCr_2O_8$. The Cr^{5+}-ions are arranged in pairs, forming dimers with a strong interaction constant J_0 between the spin-$\frac{1}{2}$ electrons inside the dimers and weaker interdimer interactions J'. For the mother compounds, $Ba_3Cr_2O_8$ and $Sr_3Cr_2O_8$, the electronic system has been reported to show a field-induced ordering phase transition which has been described in terms of a Bose-Einstein-condensation (BEC) of magnetic quasiparticles (triplons) [1, 2] which are formed by the above described dimerized electronic spins in the lattice. The critical field above which this condensation occurs depends largely on the value of J_0.

For $Ba_{3-x}Sr_xCr_2O_8$, J_0 varies in a peculiar way with Sr content x [3]. Based on a neutron-diffraction analysis of the structural properties at room temperature and at $T = 2\,\mathrm{K}$, we could show that the stoichiometry dependent disorder leads to a gradual suppression of a structural phase transition in $Ba_{3-x}Sr_xCr_2O_8$ which strongly influences the magnetic properties of the spin system, allowing us to explain these results [4].

As the change of the magnetic interactions should also modify the critical fields B_c for the magnetic ordering ($B_c \approx 12.5\,\mathrm{T}$ in $Ba_3Cr_2O_8$ and $B_c \approx 30.5\,\mathrm{T}$ in $Sr3Cr_2O_8$), we have performed low temperature magnetometry experiments in high magnetic fields. To estimate the dependence of B_c on x, we have performed pulsed field magnetometry experiments in fields up to 65 T at the *Hochfeld-Magnetlabor Dresden-Rossendorf* for x in the range 2.5 - 3.0. As the phase transition of the spin system is supposed to be of second order, the derivative $\rho(B)$ of the measured susceptibility $\chi(B)$ should peak at the transition field. In Fig. 13.2, we have plotted $\rho(B) = \mathrm{d}^2M/\mathrm{d}B^2 = \mathrm{d}\chi/\mathrm{d}B$. Note that $B_c(x)$ increases with x.

The variation of B_c due to the variation of the magnetic interactions with x should be accompanied by a shift of the critical temperature $T_c(B)$ of the magnetic ordering. To examine T_c in more detail, we have performed cantilever magnetometry experiments in high magnetic

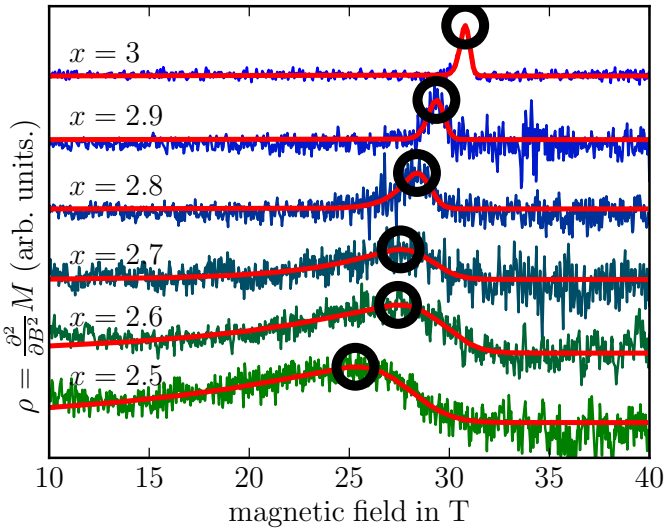

FIG. 13.2 – The derivative $\rho \equiv \mathrm{d}\chi/\mathrm{d}B$ of the susceptibility χ versus applied magnetic field B, for several compositions of $Ba_{3-x}Sr_xCr_2O_8$. Results from pulsed field magnetometry experiments at $T \approx 1.5\,K$. The black circles indicate the extrema which mark the value of the critical field B_c.

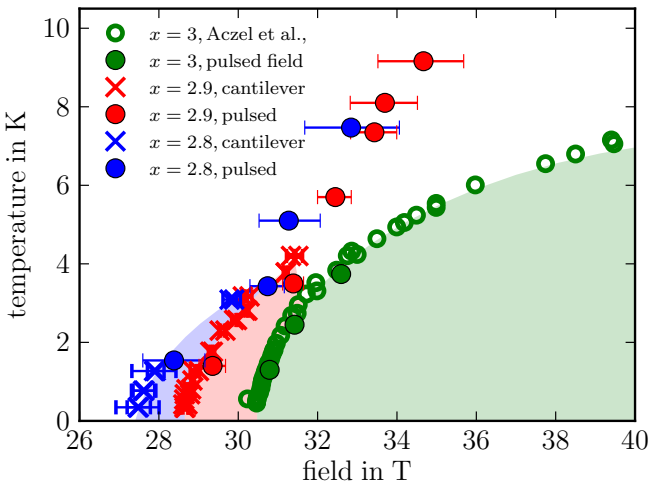

FIG. 13.3 – The critical temperature T_c for the triplon condensation as a function of the applied magnetic field for $x \in \{3, 2.9, 2.8\}$. The open circles represent data points from [2]. The colored areas are guides to the eye only.

fields at temperatures down to $T = 350\,\mathrm{mK}$ for x=2.8 and x=2.9. From the second derivative of the obtained magnetization M we have calculated $\rho(B) = \mathrm{d}^2M/\mathrm{d}B^2$. The critical field corresponds to the value at which $\rho(B)$ reaches its maximum, as in the above described pulsed field experiments.

In Fig. 13.3, we have plotted $T_c(B)$, resulting from these measurements for $Ba_{0.1}Sr_{2.9}Cr_2O_8$, $Ba_{0.2}Sr_{2.8}Cr_2O_8$ and pure $Sr_3Cr_2O_8$. The observed phase boundaries are shifted towards lower magnetic fields when lowering x, in accordance with Fig. 13.2. To verify these results from magnetometry experiments, we are currently performing high field heat capacity experiments for $x = 2.9$.

[1] M. Kofu *et al.*, Phys. Rev. Lett., **102**, (2009) 177204.

[2] A. A. Aczel *et al.*, Phys. Rev. Lett., **103**, (2009) 207203.

[3] H. Grundmann, A. Schilling, C. A. Marjerrison, H. A. Dabkowska, B. D. Gaulin, Mat. Res. Bull. **48**, (2013) 3108.

[4] H. Grundmann, A. Schilling, M. Medarde, D. Sheptyakov, Phys. Rev. B., **90**, (2014) 075101.

13.2 Superconductivity and correlated Fermi liquid behavior in noncentrosymmetric $Ca_3Ir_4Ge_4$

Inversion symmetry is an important concept for understanding superconductivity, allowing to classify superconductors by the order parameter symmetry as conventional (*s*-wave) or unconventional (*p*-, *d*-, *f*-wave). However, for structures lacking inversion symmetry, the classification loses its strict meaning and parity-violating superconductivity is allowed. Thereby, a mixture of spin-singlet and spin-triplet pairing states within the same orbital channel can occur (see, e.g., [1, 2]).

$CePt_3Si$, the most discussed noncentrosymmetric superconductor, displays pronounced unconventional properties, such as the coexistance of magnetism and superconductivity, the large H_{c2}, and a very unusual spin-relaxation rate $1/T_1$. $CePt_3Si$ is, however, also a heavy-fermionic superconductor, so its unconventional properties may not only come from the lack of inversion symmetry [3]. Other noncentrosymmetric compounds with indications for unconventional superconducting properties are Li_2Pt_3B, Mo_3Al_2C, and $LaNiC_2$. In the other noncetrosymmetric superconductors, s-wave pairing appears to be dominant and no unconventional properties were observed [4]. To improve our understanding it is important to explore novel types of noncentrosymmetric superconductors.

The cubic noncentrosymmetric $Na_3Pt_4Ge_4$ structure-type with the space group $I\bar{4}3m$, is a rather rare structure with only five known examples: $Na_3Pt_4Ge_4$ [5], $Eu_3Ni_4Ga_4$ [6], $Ca_3Ir_4Si_4$ [7], $Sr_3Ir_4Sn_4$ [8], and $Ca_3Ni_4Ga_4$ [9]. So far a detailed study has been performed for $Eu_3Ni_4Ga_4$ [10] only and electronic structure calculations only exist for $Sr_3Ir_4Sn_4$ [8].

We have now reported [11] the discovery, the crystal structure, and the elementary physical properties of $Ca_3Ir_4Ge_4$, which is a new member of the $Na_3Pt_4Ge_4$ structure type. We show that this compound is a low-temperature superconductor, while above T_c it is a paramagnetic metal, with Fermi liquid behavior, showing indications of strong electron-electron correlation.

In Fig. 13.4, we show the powder x-ray diffraction pattern at ambient temperature of a sample with the nominal composition $Ca_3Ir_4Ge_4$. The compound is found to crystallize in the $Na_3Pt_4Ge_4$ structure type with the cubic body centered $I\bar{4}3m$ space group with the lattice parameter $a = 7.56895(4)$ Å. The material is found to be air sensitive and a small CaO impurity (2%) is observed in the x-ray diffraction pattern, but all other experimentally observed intensities are in very good agreement with the $Na_3Pt_4Ge_4$ structure type. The crystal structure of $Ca_3Ir_4Ge_4$ is shown in Fig. 13.5a. The Ir atoms are surrounded by the Ge atoms in a tetrahedral coordination. These edge-sharing and corner-sharing $IrGe_4$ tetrahedra form a 3D network. The channels in the structure are occupied by Ca atoms; this channel-type array resembles that found in $NaPd_3Ge_2$ and $NaPd_4Si_4$ and related structures [12, 13]. The Ir-Ge framework consists of Ir_4Ge_4 polyanions built from tetrahedral stars, as shown in Fig. 13.5b. These tetrahedral stars do not contain any interstitial atoms, as expected from the short Ir-Ir distance.

In Fig. 13.5c, we show the Ir tetrahedron found both at the center and at the origin of the unit cell of the compound. The tetrahedral structural motifs present, and

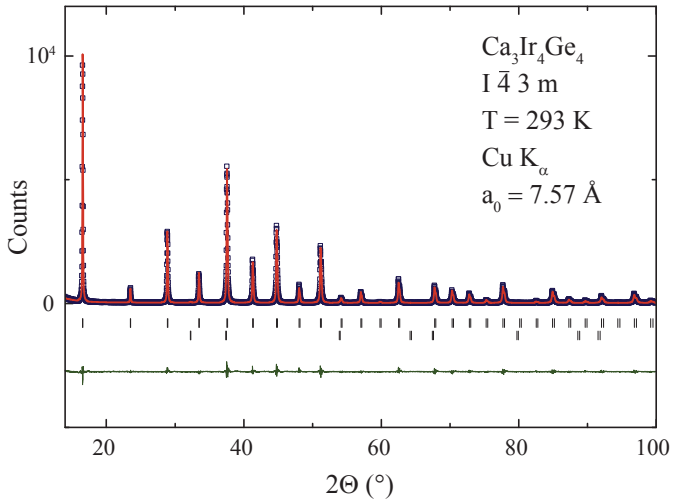

FIG. 13.4 – Powder x-ray diffraction pattern of $Ca_3Ir_4Ge_4$ at room temperature. Dark-blue squares: measurement; red curve: calculation; upper tic marks: calculated peak positions for $Ca_3Ir_4Ge_4$; lower tic marks: same for 2% CaO impurity; lower curve, difference between observed and calculated pattern.

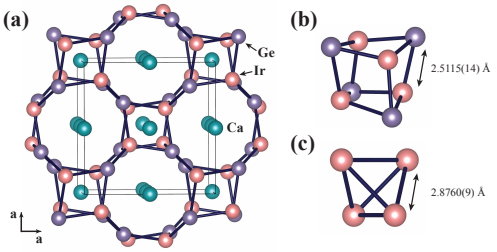

FIG. 13.5 – (a) Crystal structure of $Ca_3Ir_4Ge_4$, the Ge-Ir bonds are depicted, (b) Ir_4Ge_4 polyanion in the shape of a tetrahedral star, (c) Ir tetrahedron in the center of the unit cell.

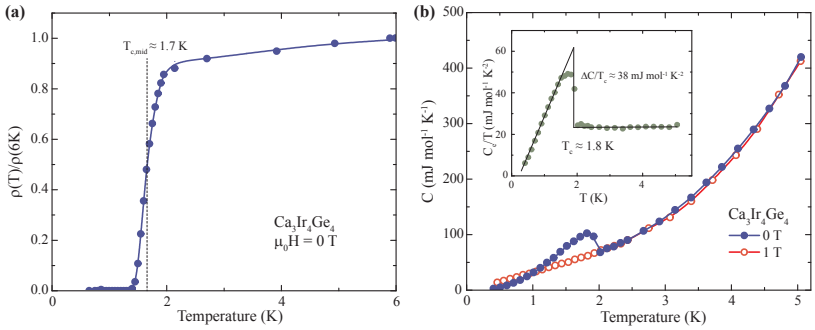

FIG. 13.6 – Low-temperature resistivity and specific heat measurements on a polycrystalline sample of $Ca_3Ir_4Ge_4$ in the vicinity of the superconducting phase transition.

their arrangement in the cell, result in $Ca_3Ir_4Ge_4$ having a noncentrosymmetric crystal structure.

In Fig. 13.6, we present the normalized resistivity $\rho(T)/\rho(6\text{ K})$ of $Ca_3Ir_4Ge_4$ in zero external magnetic field and in a temperature range 0.6 - 6 K. A clear transition to superconductivity is observed, with a critical temperature mid-point of $T_{c,mid} \approx 1.7$ K, reaching zero resistance at $T_c(\rho = 0) \approx 1.4$ K. The bulk nature of the superconductivity, confirmed by the specific heat (see Fig. 13.6b), is suppressed in an external magnetic field of $\mu_0 H = 1$ T.

Based on the Debye model and Fermi statistics the specific heat of the normal state can be calculated according to

$$C = C_e + C_l = \gamma T + \beta T^3,$$

where, γ and β denote the electronic and the phonon contributions, respectively. The electronic contribution is, under the assumption of a degenerate electron gas of non-interacting particles, linear in the density of states at the Fermi-level $D(E_F)$:

$$\gamma = \frac{\pi^2}{3} k_B^2 D(E_F).$$

With $k_B \approx 1.38 \times 10^{-23}$ J·K^{-1}, we obtain for $Ca_3Ir_4Ge_4$ with $\gamma \approx 25$ mJ $\cdot$ mol^{-1} $\cdot$ K^{-2} a $D(E_F) \approx 10.6$ states/eV, and with $\beta \approx 1.64 \cdot$ mJ $\cdot$ mol^{-1} $\cdot$ K^{-4} a Debye temperature of $\Theta_D \approx 235$ K.

In the inset of Fig. 13.6b, we show the measured C_e/T data after subtraction of the phonon contribution. The superconducting transition temperature is determined to be $T_c \approx 1.8$ K, by an entropy conserving construction (solid line in the inset of figure 13.6b), in agreement with the transition temperature observed in the resistivity measurement. The discontinuity at T_c is found to be $\Delta C/T_c \approx$ 38 mJ·mol^{-1}·K^{-2}, in good agreement with comparable intermetallic compounds. For the normalized discontinuity in the specific heat, we obtain a value of $\Delta C/\gamma T_c \approx$ 1.52, which is close to the standard weak-coupling BCS value of $\Delta C/\gamma T_c = 1.43$. Well above T_c, the compound is a paramagnetic metal, with Fermi liquid behavior (data not shown). The value of the Kadowaki-Woods ratio and Stoner enhancement factor indicate a significant electron-electron correlation in this compound.

In conclusion, we have synthesized a new compound $Ca_3Ir_4Ge_4$ by high-temperature solid-state synthesis in the noncentrosymmetric $Na_3Pt_4Ge_4$ structure type. We observe a clear transition to superconductivity below 2 K in the resistivity and in the specific heat. The physical properties display indications for electron-electron correlation and correlated Fermi-liquid behavior. Therefore, $Ca_3Ir_4Ge_4$ is a new candidate material for the investigation of the admixture of spin-singlet and spin-triplet pairing states in noncentrosymmetric superconductors.

[1] M. Sigrist, K. Ueda, Rev. Mod. Phys. **63** (1991) 239.

[2] E. Bauera and M. Sigrist, *Non-Centrosymmetric Superconductors*, (Springer-Verlag, Berlin, Heidelberg, 2012).

[3] E. Bauer *et al.*, Phys. Rev. Lett. **92** (2004) 027003.

[4] M. Isobe *et al.*, Chemistry of Materials **26** (2014) 2155, and citations therein.

[5] W. Thronberens and H. Schuster, Z. Naturforsch. B **34** (1979) 781.

[6] A. E. Dwight, Materials Research Bulletin **22** (1987) 305.

[7] S. Schoolaert and W. Jung, ZAAC **628** (2002) 1806.

[8] R. Hoffmann *et al.*, International Journal of Inorganic Materials **2** (2000) 135.

[9] S. Kim *et al.*, Dopov. Akad. Nauk Ukr. RSR, Ser. B, 13, (1983).

[10] C. Anupam *et al.*, J. Phys.: Condens. Matter **24** (2012) 326002.

[11] F. von Rohr *et al.*, Phys. Rev. B **89** (2014) 224504.

[12] W. Thronberens *et al.*, Journal of the Less-Common Metals **76** (1985) 99.

[13] M. N. Ali, F. von Rohr, C. Campana, A. Schilling, R. J. Cava, *to be published*.